MATERIALS SCIENCE

A thin, deformable, high-performance supercapacitor implant that can be biodegraded and bioabsorbed within an animal body

Hongwei Sheng[1]*, Jingjing Zhou[1]*, Bo Li[1], Yuhang He[2], Xuetao Zhang[1], Jie Liang[1], Jinyuan Zhou[1], Qing Su[1], Erqing Xie[1], Wei Lan[1,3†], Kairong Wang[2†], Cunjiang Yu[3†]

Copyright © 2021 The Authors, some rights reserved; exclusive licensee American Association for the Advancement of Science. No claim to original U.S. Government Works. Distributed under a Creative Commons Attribution NonCommercial License 4.0 (CC BY-NC).

It has been an outstanding challenge to achieve implantable energy modules that are mechanically soft (compatible with soft organs and tissues), have compact form factors, and are biodegradable (present for a desired time frame to power biodegradable, implantable medical electronics). Here, we present a fully biodegradable and bioabsorbable high-performance supercapacitor implant, which is lightweight and has a thin structure, mechanical flexibility, tunable degradation duration, and biocompatibility. The supercapacitor with a high areal capacitance (112.5 mF cm^{-2} at 1 mA cm^{-2}) and energy density (15.64 μWh cm^{-2}) uses two-dimensional, amorphous molybdenum oxide (MoO_x) flakes as electrodes, which are grown in situ on water-soluble Mo foil using a green electrochemical strategy. Biodegradation behaviors and biocompatibility of the associated materials and the supercapacitor implant are systematically studied. Demonstrations of a supercapacitor implant that powers several electronic devices and that is completely degraded after implantation and absorbed in rat body shed light on its potential uses.

INTRODUCTION

Critical medical needs have driven the development of biodegradable, implantable medical electronics (BIMEs) that can provide medical diagnostic and therapeutic functions over a certain period of time and then disintegrate to dissolve without surgical removal (*1*–*4*). Fast technological advances in BIMEs, such as a pacemaker and neurostimulator, have been achieved over the past few years with the recent advancement in materials development, electronics technologies, and mechanical designs. However, one of the standing challenges is the lack of a proper implantable power source, which needs to have sufficient capacity to power the BIMEs, mechanical softness to be compatible with soft organs and tissues, compact form factors, and biodegradability to only remain for a desired time frame. Reported implantable power source solutions include batteries (*5*), wireless power transfer modules (*6*, *7*), and energy harvesters (*8*, *9*). For instance, conventional batteries have been integrated with the BIMEs to power them (*10*). Wireless power transfer device based on inductive coupling with coils has been shown to transfer electrical energy into the body from outside in an untethered manner (*6*). Triboelectrical energy generators have been demonstrated to efficiently harvest organs' mechanical motions into electrical energy (*8*). However, these devices have certain deficiencies, such as their nonbiodegradability, mechanical rigidity (incompatibility with soft organs and tissues), and relatively large form factors, thus limiting their usage as a biodegradable power source. On the other hand, a few recent studies on degradable batteries and supercapacitors have been reported (*11*–*17*) to serve as biodegradable and bioabsorbable counterparts. However, some critical shortcomings exist. For instance, they are not proven or readily fully biodegraded and bioabsorbed within animal bodies, have relatively low electrochemical performances (energy and/or power densities), and/or have inappropriate form factors and are mechanically rigid, thus impeding the suitability of implantation. Therefore, fully biodegradable and bioabsorbable high-performance energy devices are sought.

Here, we report a mechanically deformable, fully biodegradable, high-performance supercapacitor implant, which can be biodegraded and bioabsorbed within animal bodies. The supercapacitor implant uses two-dimensional, defective amorphous molybdenum oxide (MoO_x) flakes on Mo foil as a binder-free pseudocapacitance electrode, which is directly synthesized on water-soluble Mo foil using an all-green, controlled electrochemical oxidation approach. The unique MoO_x flake–based electrode renders high electrochemical performance and biodegradation simultaneously. The fully biodegradable supercapacitor implant has high areal capacitance (112.5 mF cm^{-2} at 1 mA cm^{-2}) and excellent energy density (15.64 μWh cm^{-2})/high power density (2.53 mW cm^{-2}). The life span of supercapacitor implants can be engineered to vary from a few days to a few weeks. The biodegradable supercapacitor implant can be disintegrated through a series of metabolic and hydrolytic reactions, and the resulting by-products can be bioabsorbed into the body without any adverse long-term effects. Supercapacitor device construction and characterization, dissolution kinetics, biocompatibility studies, and biodegradation/bioabsorbability investigations in Sprague-Dawley (SD) rats and in vitro reveal key aspects of the supercapacitor implant.

RESULTS

Supercapacitor implant and MoO_x flake electrodes

As illustrated in Fig. 1A, the developed biodegradable supercapacitor implant has a sandwich construction, including Mo foil (current

[1]Key Laboratory of Special Function Materials and Structure Design, Ministry of Education, School of Physical Science and Technology, Lanzhou University, Lanzhou 730000, People's Republic of China. [2]Key Laboratory of Preclinical Study for New Drugs of Gansu Province, School of Basic Medical Sciences, Lanzhou University, Lanzhou 730000, People's Republic of China. [3]Department of Mechanical Engineering, Texas Center for Superconductivity, University of Houston, Houston, TX 77204, USA.
*These authors contributed equally to this work.
†Corresponding author. Email: lanw@lzu.edu.cn (W.L.); wangkr@lzu.edu.cn (K.W.); cyu15@uh.edu (C.Y.)

collector), MoO_x flakes, and sodium alginate (Alg-Na) gel electrolyte. Specifically, a one-step electrochemical oxidation approach is used to obtain defective, amorphous MoO_x flakes grown in situ on Mo foil to serve as a binder-free pseudocapacitive electrode. In addition, the corresponding preparation procedure is given in Materials and Methods. Such an electrochemical route is all green, controlled, and universal, requiring no additional chemicals and posttreatments. As for the electrolyte (Fig. 1B), biodegradable Alg-Na gel consists of α-L-guluronic acid (G) and β-D-mannuronic acid (M) residues linked by one to four glycosidic bonds, forming polymeric blocks (GG blocks, MM blocks, and GM blocks). The fabricated biodegradable, symmetric solid-state supercapacitor implant based on MoO_x flakes is lightweight, very thin (~30 μm), and mechanically flexible, as demonstrated by wrapping around a finger (Fig. 1C).

Anodization to form MoO_x flakes was carried out by applying the alternating voltage between 0 and 1 V in aqueous NaCl electrolyte at room temperature. When Mo foil was applied with a varying sawtooth voltage based on a cyclic voltammetry (CV) sweep in a three-electrode electrochemical configuration, an oxidation reaction ($Mo \rightarrow Mo^{x+} + xe^-$) is activated, and a counterreaction occurs at the cathode ($xH_2O + xe^- \rightarrow \frac{x}{2}H_2\uparrow + xOH^-$). The growth of an anodic oxide layer can be regulated by altering the electrolyte anions and the given anodization parameters, such as potential windows, scan rates, and cycling numbers. Three possible chemical reactions take place at the interfacial (solid/liquid) sites during the anodization process (*18*): (i) Mo foil is continuously dissolved, corroded, and electropolished (fig. S1); (ii) the as-formed Mo^{x+} ions react with O^{2-} (provided by deprotonation of H_2O or OH^- in the electrolyte) to produce a compacted oxide layer; and (iii) the competitive reaction is established between dissolution and oxide construction. The polished Mo foil (thickness, 20 μm) has a relatively smooth surface, as shown in Fig. 2A. After anodization, the top-view and cross-sectional scanning electron microscopy (SEM) images (Fig. 2, B and C, and fig. S2, A and B, respectively) of Mo foil collectively reveal the surface morphology of derived dendrite flakes. During continuous electrochemical cycling, the interconnected MoO_x flakes crack into microsized blocks because of the built-in stress induced by the volume change, as shown schematically in fig. S3. It is noted that such electrochemically derived MoO_x flakes are distinct from the existing report (*16*) in terms of (i) the synthesis parameters and steps, (ii) the yielded electrode compositions and surface morphology, and (iii) electrochemical performances.

It is worth mentioning that these cracks can fill with Alg-Na gels and facilitate the sufficient contact between electrolyte ions and MoO_x flakes, broadly enhancing electrochemical performances. MoO_x flakes are typically 4 to 10 μm in length and ~1 μm in thickness. Upon peeling off via a scotch tape, the unique interface stacking structure between MoO_x flakes and Mo foil could be directly

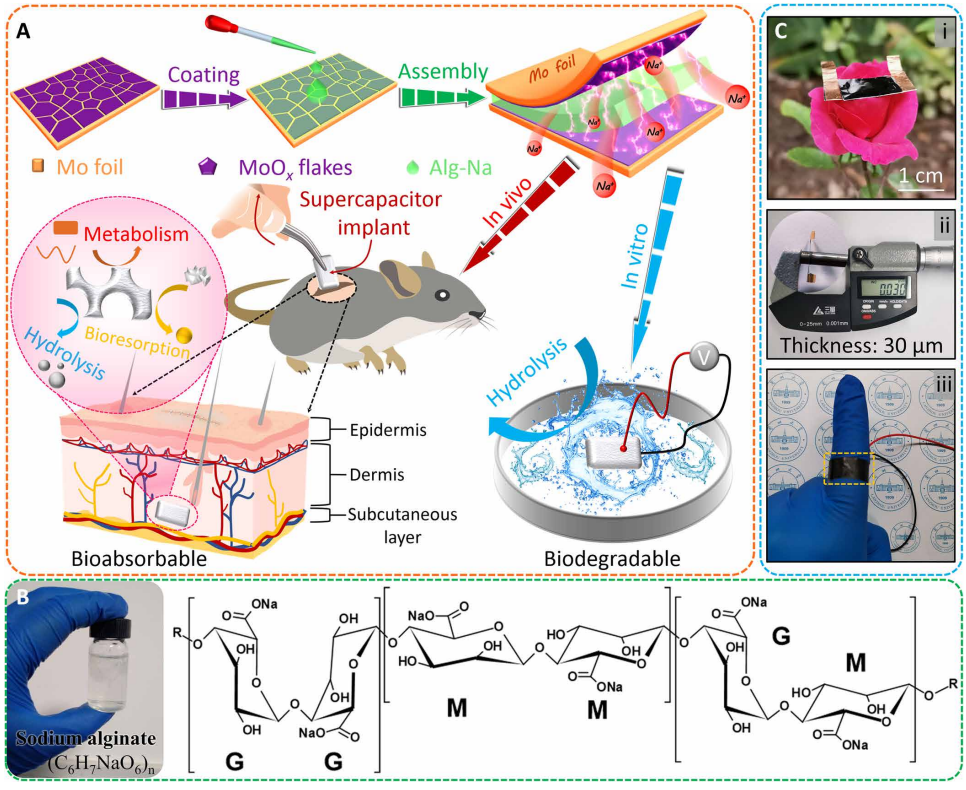

Fig. 1. Deformable, fully biodegradable supercapacitor implant. (**A**) Schematic illustration of the fabrication process and applications of the fully biodegradable supercapacitor implant. As for the implanted supercapacitor device in vivo and in vitro, biodegradable polylactic acid (PLA)/polyvinyl alcohol (PVA) and/or starch paper are used to encapsulate the edges and external. After completion, the encapsulated supercapacitors can be absorbed in vivo and degraded in vitro at a certain rate. (**B**) Photograph of the prepared Alg-Na gel electrolyte and chemical structure of M (mannuronate) and G (guluronate) units of Alg-Na. (**C**) Optical images of the lightweight and deformable supercapacitor implant when placed on a flower and wrapped around a finger, and its thickness measured by an electronic helical micrometer. Photo credit: Hongwei Sheng, Lanzhou University.

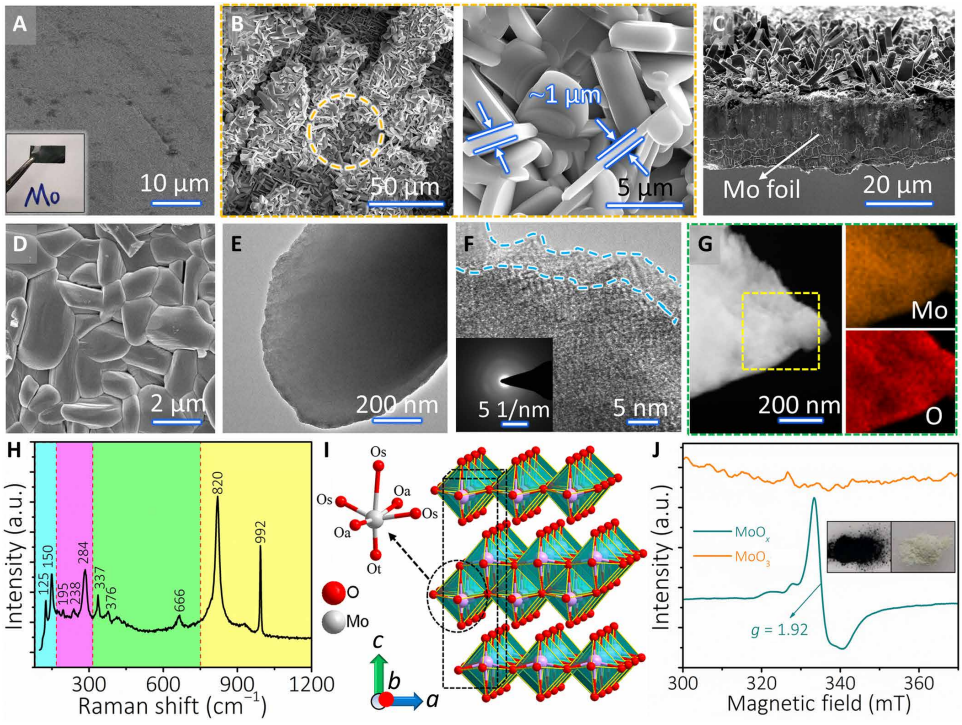

Fig. 2. Morphological and structural characterization of the MoO_x electrode. (**A** and **B**) SEM images of (A) the polished Mo foil and (B) SEM image of the MoO_x electrode. (**C**) Cross-sectional SEM images of MoO_x electrode. (**D**) SEM images of the contact surface between MoO_x flakes and inner Mo foil. (**E** and **F**) TEM and high-resolution TEM (HRTEM) images of the delaminated MoO_x flakes, respectively. The inset in (F) shows the corresponding selected-area electron diffraction (SAED) pattern. (**G**) Acquired energy-dispersive spectroscopy (EDS) elemental mapping of MoO_x flakes. (**H**) Raman spectrum of MoO_x electrodes. a.u., arbitrary unit. (**I**) Crystal structure of α-MoO_3, representing the layered structure and three types of oxygen anion. (**J**) ESR spectra of MoO_x and MoO_3. Inset: Digital photographs of MoO_x (left) and MoO_3 (right) powders. Photo credit: Hongwei Sheng, Lanzhou University.

observed in Fig. 2D. The as-prepared MoO_x flakes were grown in situ and firmly adhered to a Mo foil current collector, which naturally derives a low contact resistance between MoO_x flakes and Mo foil and also alleviates the exfoliation of active materials during the electrochemical reactions. In addition, the anodized MoO_x flakes have a layered structure with many surface and edge defects, as observed by transmission electron microscopy (TEM) images (Fig. 2, E and F, and marked with red circles in fig. S2, C and D). These defects can anchor more exotic ions during the reaction process owing to the exposed active sites, which is very beneficial to improve the electrochemical performances. The amorphous structure of MoO_x flakes is confirmed on the basis of the characteristic halo rings from selected-area electron diffraction (SAED) (inset of Fig. 2F), and a broad wave peak exists in x-ray diffraction (XRD) pattern (fig. S4A). The corresponding elemental mapping images in Fig. 2G show that Mo and O elements are uniformly distributed in a whole MoO_x flake, in good agreement with the acquired energy-dispersive x-ray analysis (fig. S4B).

The micro-zone Raman spectrum further reveals that the structural characteristics of amorphous MoO_x flakes agree with the orthorhombic phase (α-MoO_3) with a *Pbnm* space group. In Fig. 2H, the Raman shift peaks correspond to translational rigid-chain (T_c) (125 cm^{-1}) and rotational rigid-chain (R_c) (150 cm^{-1}), O═Mo═O twisting (195 cm^{-1}) and wagging (284 cm^{-1}), O—Mo—O bending (337 cm^{-1}), scissoring (376 cm^{-1}), and stretching (666 cm^{-1}) vibration modes for α-MoO_3 (*19*, *20*). The broadened bands at 820 and 992 cm^{-1} (Ag, terminal Mo═O stretch) might be attributed to the local distortion of the M—O polyhedra due to oxygen vacancies, which, in turn, influences the lattice vibrations (*21*). As illustrated in Fig. 2I, the structural framework of α-MoO_3 consists of a bilayer network of edge-sharing MoO_6 octahedra as building units. The bilayers are further stacked and piled up along the *c* axis and bonded to adjacent layers by van der Waals (vdW) forces (*22*). There are three configurations of oxygen anion, including the "terminal oxygen" (O_t), the O_a that forms asymmetric bonds with two Mo ions in the *b* axis, and "symmetric oxygen" (O_s) with threefold symmetry. The corresponding x-ray photoelectron spectroscopy (XPS) survey spectrum can be found in fig. S4C. From the deconvoluted spectrum of Mo 3d core level (fig. S5), the most intense duplet located at 235.7 and 232.6 eV is well matched with Mo $3d_{3/2}$ and Mo $3d_{5/2}$ in the Mo^{6+} oxidation state, respectively (*23*, *24*). Besides, four minor peaks of Mo 3d spectrum originate from lower oxidation states of Mo, which are ascribed to Mo^{5+} (234.3 and 232.2 eV), Mo^{4+} (231.2 eV), and metallic Mo^0 (231.8 eV) (*25*). The presence of metallic Mo^0 in MoO_x flakes is further verified by Mo 3d spectrum of pure Mo foil (fig. S4D). For the high-resolution O 1s spectrum (fig. S5), three deconvoluted peaks at 530.8 and 530.4 eV arise from the bridging oxygen of Mo—O—Mo in MoO_x flakes (*25*). Moreover, another peak at 532.4 eV can be attributed to the oxygen atoms in the vicinity of the oxygen vacancies (*26*). According to the reported density functional theory calculations (*22*), an oxygen vacancy configuration, an oxygen vacancy at the O_t site, and two Mo^{5+} bipolarons near the defect center have the lowest formation enthalpy (1.32 eV), which is easier than the formation of oxygen vacancies at the O_a and O_s sites. This is in

agreement with our measured electron spin resonance (ESR) spectra (Fig. 2J), where Mo^{5+} oxidation states are verified. Because Mo^{6+} is a d^0 species and Mo^{5+} is a d^1 species, the deep blue sample of as-synthesized MoO_x flakes shows a strong signal at $g = 1.92$ (*26*, *27*).

The oxygen vacancy concentration of MoO_x flakes was further characterized using thermal gravimetric analysis (TGA) (fig. S6). Compared to the results in argon ambiance, MoO_x flakes react with oxygen in air ambiance during heating, resulting in a lower loss of mass. From the calculations, we estimate that the form of MoO_x corresponds to $MoO_{2.81}$. Because of the existence of these oxygen vacancies, the blue MoO_x flakes also show strong light absorbance, as confirmed by ultraviolet-visible (UV-Vis) absorption spectroscopy (fig. S4, E and F). Oxygen vacancies can enlarge the vdW gap and regulate the valency state of Mo ions in amorphous MoO_x flakes, thus promoting faster charge storage kinetics and maintaining the layered structure well during the insertion and removal of small ions (*21*, *28*). All these results conclusively validate the successful synthesis of the defective MoO_x flakes on Mo foil. A proposed mechanism (illustrated in fig. S7) depicts the interface reactions, which are analogous to the corrosion and passivation behaviors of Mo reported elsewhere (*29*, *30*). After initiation, a thin and conductive Mo^{4+} oxide film (e.g., MoO_2) grows at its interface with the Mo metal ($Mo + 2H_2O \rightarrow MoO_2 + 4e^- + 4H^+$). The growth of a new Mo^{5+} and Mo^{6+} anodic oxide layer (e.g., Mo_2O_5 and MoO_3) depends on the migration rate of the field-assisted electronic/ionic transport [Mo cation (V_{Mo})/oxygen vacancies (V_O), etc.] through the MoO_2 layer. At the same time, oxide film dissolution may occur at the oxide-electrolyte interface ($MoO_3 + 2OH^- \rightarrow HMoO_4^- + H_2O + e^-$), followed by the formation of soluble species (e.g., $HMoO_4^-$ and MoO_4^{2-}). Under a cyclic varying voltage (U), the field $F = U/d$ regularly drops, thereby lowering the driving force for ion migration with increasing oxide film thickness (d). Last, a mixed-valence and stable oxidation layer with a finite thickness is reached, which mainly relies on the anodization voltage (*18*), consistent with the XPS results (fig. S8). To achieve a high-performance MoO_x electrode, the effect of the anodization parameters, such as potential windows, scan rates, and cycling numbers, on their electrochemical performances was further investigated. We manipulate the chemical composition and morphology of active materials (MoO_x flakes) to achieve optimum electronic/ionic transport kinetics. Detailed results are shown in figs. S9 to S11. On the basis of these experimental results, an optimized anodization condition (0.1 V s^{-1}, 0 ~ 0.8 V, 150 cycles) was chosen in the following studies.

Electrochemical characterization of MoO_x electrodes

The electrochemical properties of the optimized MoO_x electrodes were evaluated using a standard three-electrode setup with a 1 M NaCl aqueous electrolyte. Compared with the MoO_x electrode, it can be found that the CV curve (10 mV s^{-1}) of the pure Mo foil approaches a line, showing a negligible capacitance contribution (Fig. 3A). The CV shapes of the MoO_x electrode are well maintained even up to a scan rate of 1 V s^{-1} (Fig. 3B), exhibiting the rapid current response upon applied voltage reversal and highly pseudocapacitive behavior in the MoO_x electrode. This was also verified by the galvanostatic charge-discharge (GCD) curves (Fig. 3C). As the molybdenum oxide is an intercalation-type pseudocapacitive material, its intercalation typically shows a transitional behavior between supercapacitors and batteries. It is noted that the electrochemical features are similar to those of the carbon-based materials (*31*–*33*). As expected, the areal capacitances derived from the CV and GCD profiles are comparable, reaching the highest capacitance of 227.4 mF cm^{-2} at 2 mA cm^{-1} (Fig. 3D). For MoO_x flakes in NaCl aqueous electrolyte, the Faradic redox reactions involve both surface adsorption and desorption, as quantitatively illustrated in Eq. 1. Besides, the intralayer and interlayer (width of vdW gap, 0.69 nm) of this crystal structure allow intercalation/deintercalation (Eq. 2) of some small ions (*34*), such as Na^+ ions (ionic radius, 0.102 nm). There are two distinguishable Na^+ intercalation sites (illustrated in Fig. 3E). Charge storage occurs mainly by the Na^+ insertion into the interlayer site to form sodium MoO_x (Na_yMoO_x) (*23*, *33*)

$$(Mo^{2x}O_x)_{surface} + Na^+ + e^- \longleftrightarrow (Mo^{2x-1}O_xNa)_{surface} \quad (1)$$

$$MoO_x + ye^- + yNa^+ \leftrightarrow Na_yMoO_x \quad (2)$$

On the other hand, oxygen vacancy defects in MoO_x flakes not only act as storage/absorption sites for anchoring more Na^+ ions but also reduce the stress and electrostatic repulsion between adjacent layers during the intercalating process of Na^+ ion (*28*). A capacitance retention of 92.7% was achieved after 500 cycles (Fig. 3F), showing excellent short-term cyclic performance. The observed straight line in the electrochemical impedance spectroscopy (EIS) curve also reveals a unique capacitive behavior of MoO_x electrodes (Fig. 3G), agreeing with the CV and GCD results. The intercept of Nyquist plot on the real axis represents R_s, reflecting the electrode conductivity. The extracted R_s value is as low as 2.75 ohms, manifesting a good conductivity and little internal resistance of the MoO_x electrode, as well as consistent interfacial contact between MoO_x flakes and Mo foil. No obvious semicircle was observed, suggesting a negligible charge transfer resistance (R_{ct}). Besides, the Nyquist plots can be well fitted with the proposed equivalent circuit in the inset of Fig. 3G. The outstanding electrochemical properties could be ascribed to the following reasons. First, the in situ growth approach guarantees good electrical interaction between active materials and current collector, avoiding the utilization of polymeric binders and conductive additives. Second, the defect-enriched flakes in a loosely packed manner with a highly open structure provide abundant storage/absorption sites for anchoring extraneous ions during the electrochemical reaction process and promote ionic diffusion and charge transfer. It is noted that the charge storage properties of MoO_x electrodes can be further optimized by altering anodization parameters, such as the electrolyte anionic species and concentration, solution temperature, and pH value, tuning vdW gap/oxygen defects/surface chemistries and morphologies. On the basis of the vast generalization of electrochemical oxidation, other water-soluble metals, such as Fe and W, can also be chosen to attempt, opening up a vast opportunity of achieving a binder-free pseudocapacitive electrode with high performance.

Performances of the supercapacitor implant

On the basis of MoO_x electrodes, deformable supercapacitors were constructed. Figure 4A shows the photographs of a flexible supercapacitor (1 cm × 2 cm), under various deformation modes (flat, bend, and roll-up). Three essential parameters (θ, R, and L) are commonly used to demonstrate the bending state of flexible energy storage devices, where θ is the bending angle, R is the bending radius, and L is the device length (*35*). Here, R and L were fixed to 0.5 and 2 cm, respectively, and θ was changed from 30° to 120°, resulting in different stress areas, as illustrated in the inset of Fig. 4B. No

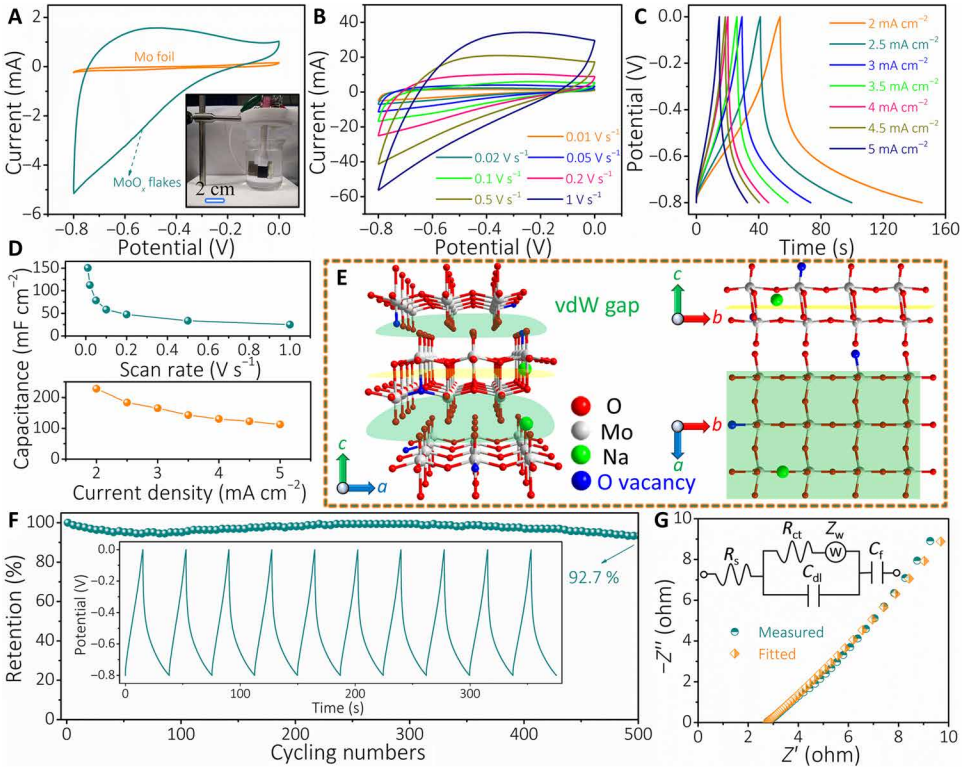

Fig. 3. Electrochemical characterization of MoO_x electrodes. (**A**) CV curves (at 10 mV s^{-1}) of Mo foil and MoO_x electrode. Inset is a standard three-electrode system. (**B** and **C**) CV curves at different scan rates and GCD curves at different current densities for MoO_x electrode, respectively. (**D**) Rate capability of MoO_x electrodes obtained from CV and GCD curves. (**E**) Possible Na^+ intercalation sites at intralayer and interlayer. (**F**) Electrochemical stability versus cycling number during 500 cycles (the inset is the typical GCD curves upon cycling). (**G**) Nyquist plot of MoO_x electrode; the plots were fitted by the proposed model of an electrical equivalent circuit in the inset. Photo credit: Hongwei Sheng, Lanzhou University.

obvious capacitance decay was found after bending at different angles and many times with 60° bending angle (Fig. 4B and fig. S12, A and B), demonstrating excellent flexibility of the as-fabricated supercapacitors. The capacitive properties of the flexible supercapacitors were investigated in an ambient environment. An appropriate combination of both high voltage window (1 V) and coulombic efficiency has been achieved, as shown in Fig. 4C and fig. S12 (C and D). Beyond a voltage of 1 V, a pointed CV tail starts to evolve with relatively low coulombic efficiency. Therefore, the potential window with 0 to 1 V was carried out in the following tests. The quasirectangular-shaped CV curves (Fig. 4D) are clearly visible at scan rates up to 1 V s^{-1}, suggesting good capacitive behavior and excellent power handling performances. Figure 4E shows that GCD profiles from 1 to 5 mA cm^{-2} are almost symmetric and linear without noticeable internal resistance drop, implying a small intrinsic series resistance and fast charge-discharge process. Besides the capacitive behavior, the emergence of a minor potential plateau further revealed the existence of a battery-type charge storage behavior of the materials. An ultrahigh capacitance of 112.5 mF cm^{-2} at 1 mA cm^{-2} is achieved, as shown in Fig. 4F. In addition, cyclic tests (Fig. 4G) showed that the capacitance of our fabricated supercapacitors started to decrease in the first 1000 cycles and then remained stable for the next 1000 cycles. This initial decrease in capacitance could be attributed to the insufficient activation of active materials. A capacitance retention of 86.7% was obtained after 2000 cycles, indicating a fairly good cyclic performance. As shown in fig. S12E, the supercapacitor has a low internal resistance of 15.58 ohms and fast ion diffusion in the Alg-Na electrolyte. On the basis of the rate performance, the calculated energy and power densities of the flexible supercapacitor are superior to existing works (Fig. 4H; see detailed data in table S2). Both energy density (15.64 μWh cm^{-2}) and power density (2.53 mW cm^{-2}) are comparable with nonbiodegradable supercapacitors and higher than those of most recently reported degradable supercapacitors, such as Fe/ZnO (*17*), oxidized Mo wire (*16*), metallic Mo (*14*), Au/MnO_2/Au (*36*), and MnO_2/Si nanowires (*37*). To further enhance the output voltage and capacitance, one feasible approach is to serially and parallelly connect multiple supercapacitors. For instance, when two identical supercapacitors were connected in series, the voltage can boost up to 2.0 V or even much higher, as shown in Fig. 4I and fig. S12F. Moreover, compared to the enclosed area of CV curves, two parallelly connected supercapacitors almost double the capacitance of a single supercapacitor. As shown in the insets of Fig. 4I, commercial light-emitting diodes (LEDs) and electronic thermometers can be powered up by connecting supercapacitors in series. Furthermore, energy density and power density can be further improved by engineering asymmetric configurations, such as biodegradable Zn and Mg foil. In this study, it primarily aims to achieve the capacity to meet the requirements of ultralow-power/voltage devices for BIMEs.

Biodegradation and bioabsorption of the supercapacitor implant

We further systematically studied its degradation characteristics. Figure 5A illustrates a series of photo images of the MoO_x electrode

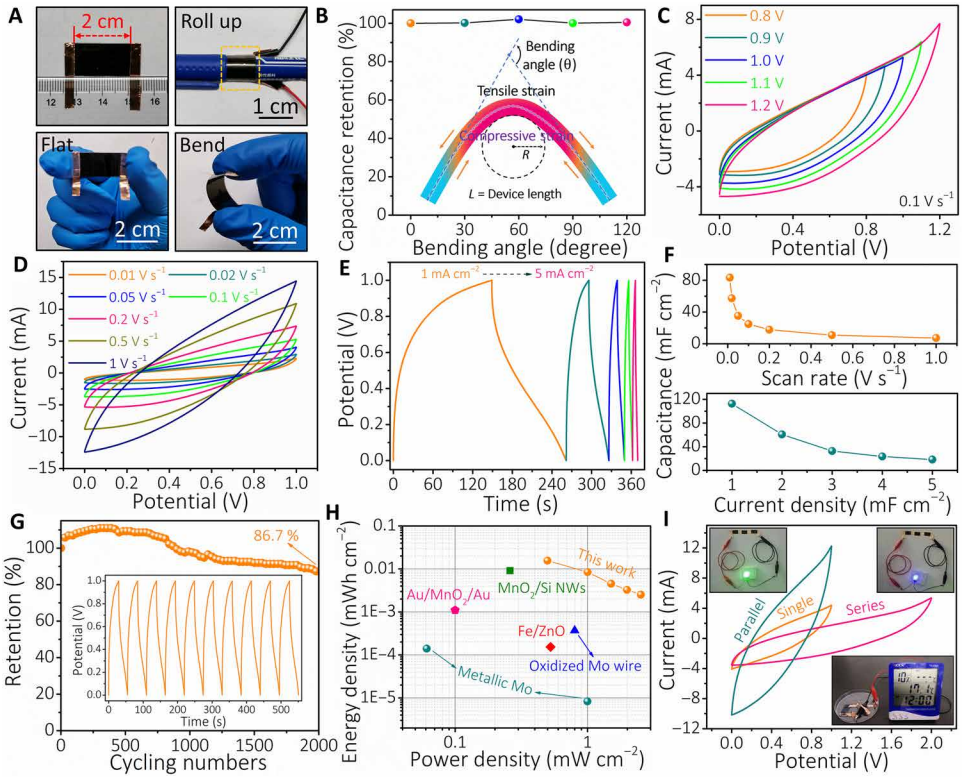

Fig. 4. Performances of the supercapacitor. (**A**) Digital photographs of a MoO_x-based supercapacitor under different conditions, indicating its flexible properties. (**B**) Capacitance retention measured under deformations. Inset: Schematic diagram of the device structure at various bending states, leading to a different stress area. (**C**) CV curves (at 0.1 V s^{-1}) at different voltage ranges for the supercapacitor. (**D**) CV curves, (**E**) GCD profiles, and (**F**) areal capacitance of the supercapacitor at different rates. (**G**) Long-term cycling of the supercapacitor at 2 mA cm^{-2}. Inset shows the typical GCD curves during cycling. (**H**) Ragone plots of the assembled supercapacitor compared with other reported ones. Detailed information is given in table S2. (**I**) CV curves of the supercapacitors in one cell, two series, and two parallel configurations; insets are digital photographs of an LED and electronic thermometer powered by the supercapacitors in series. Photo credit: Hongwei Sheng, Lanzhou University.

after immersion in phosphate-buffered saline (PBS) solution (10 mM, pH 7.4) at 37°C. It was found that MoO_x flakes were totally eliminated from the surface of Mo foil, and the inner Mo foil was exposed after 1 month, followed by a cracking corrosion morphology with small nanoparticles during the dissolution process (inset of Fig. 5B). The next 2 months witnessed new oxide layer formation on the surface and morphological transition from bulk to tiny dark powders. Meanwhile, the mass changes of MoO_x electrodes were also measured at room temperature (22°C) and at 37°C (Fig. 5B). The dissolution rates of MoO_x electrodes are calculated to be 0.15 and 0.29 mg day^{-1} at 22° and 37°C, respectively. It is noted that Mo, as an essential trace element, is vital for human nutrition. In general, the Mo content in healthy adults is about 9 mg, with a daily intake of 300 μg of Mo from the ordinary diet every day, depending on age and sex (*38*). The obtained dissolution rate at 37°C well matches the body's daily demand for Mo element. The MoO_x electrode dissolution follows the following hydrolysis reactions (*14*, *30*)

$$MoO_3 + 2OH^- \rightarrow HMoO_4^- + H_2O + e^- \quad (3)$$

$$MoO_2 + 2H_2O \rightarrow MoO_4^{2-} + 4H^+ + 2e^- \quad (4)$$

$$Mo + 4H_2O \rightarrow MoO_4^{2-} + 8H^+ + 6e^- \quad (5)$$

The dissolution rates also depend on many parameters, including surface morphology, chemical composition/ionic concentration, pH level, and solution temperature (*39*). Besides the electrodes, the dissolution behavior of the transparent Alg-Na gel electrolyte film was also examined in PBS (10 mM, pH 7.4) (see fig. S13). An Alg-Na film with an "LZU" marker was quickly dissolved within 2 hours at an elevated temperature (60°C), suggesting the dissolution essence of the gel electrolyte.

By adopting different encapsulating strategies, the average dissolution time of the supercapacitor can be tuned from days to weeks in a liquid environment. With the MoO_x electrode as a natural package, only edge encapsulating is needed. Here, two biodegradable polymers, such as polyvinyl alcohol (PVA) and polylactic acid (PLA), were selected to encapsulate and regulate the lifetime of supercapacitor for both short and long terms (Fig. 5C). Electrochemical stability of the supercapacitor encapsulated with PLA (fig. S14) was first studied in an open ambient environment [%Relative Humidity (RH) = 30%; 17.9°C]. The results showed that the encapsulated supercapacitor could operate effectively for up to 5 days. The corresponding electrochemical performance tests of the encapsulated supercapacitor were further conducted in PBS (10 mM, pH 7.4) at 37°C. Figure 5D shows the CV curves (at 0.1 V s^{-1}) in various stages for the short-term work. The areal capacitances derived from the CV profiles are plotted as a function of dissolution time, shown in Fig. 5E. The capacitance reaches a peak (24.8 mF cm^{-2}) on the second

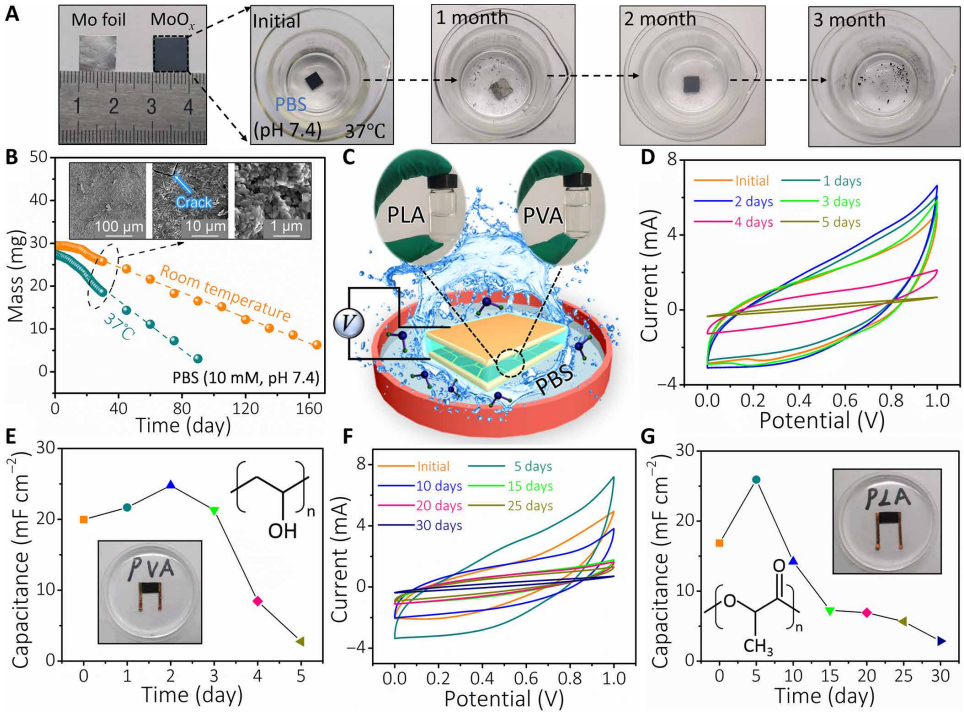

Fig. 5. Degradability of MoO_x electrodes and electrochemical performances of the supercapacitors in PBS. (**A**) Photographs of the time-sequential dissolution of a single MoO_x electrode (1 cm × 1 cm) immersed in PBS (pH 7.4) at 37°C. (**B**) Mass change of MoO_x electrode (20 μm thick) as a function of elapsed time in PBS solution (at room temperature and 37°C). Inset is an SEM image of MoO_x electrode during dissolution. (**C**) Schematic of encapsulated supercapacitors in PBS solution at 37°C. Electrochemical properties of supercapacitors for (**D** and **E**) a short-term work and (**F** and **G**) a long-term work. Insets are the corresponding molecular formula and photographs. Photo credit: Hongwei Sheng, Lanzhou University.

day, coincided with the GCD results (fig. S15A). This initially increased capacitance mainly attributes to water molecules and ion infiltration in PBS solution and corrosion of inner Mo foil (*17*). While the former enhances the ionic conductivity in the Alg-Na gel electrolyte, the latter provides an additional faradaic pseudocapacitance. As excessive water molecules are infiltrated into Alg-Na gel electrolyte, the structural stability of the supercapacitor would be destroyed, resulting in a subsequently reduced capacitance. The EIS curves of the supercapacitor further support the capacitance change at various stages (fig. S15B). Initially, the improved ionic conductivity causes the decrease of overall resistance R_s from the original 11.2 to 5.5 ohms on the second day. However, the deep dissolution of Alg-Na gel into PBS solution and the gradual shedding of active layer (MoO_x flakes) from the current collector are accompanied by the supercapacitor structural detachment, eventually leading to the enhanced R_s (26.0 ohms) and the reduced slope of EIS curves. For the long-term work, the efficient, workable time of the PLA-encapsulated supercapacitors can be prolonged to 30 days (Fig. 5, F and G), which can be attributed to the slower dissolution nature of the PLA polymer. The trend of capacitance change is similar to the above-depicted PVA-encapsulated biodegradable supercapacitor. The maximum areal capacitance reaches 25.9 mF cm^{-2} on the fifth day, agreeing with GCD results in fig. S15C. The subsequently reduced capacitance can be attributed to the damage of electrode and device structure, hydrolysis of PLA-encapsulating layer, and electrolyte loss due to long-term immersion, which is also further confirmed by EIS plots (see fig. S15D). It is worth mentioning that the desired functional lifetime could be further engineered by either controlling its thickness, microstructure, chemistry, and molecular weight of the encapsulating layer and/or exploring other biodegradable encapsulating materials. These results suggest that the degradable supercapacitor could serve as an ideal biodegradable power source for BIMEs.

The biocompatibility of the constituent materials and the products of dissolution are critically important for applications in BIMEs. Previously reported works had confirmed the excellent biocompatibility of Mo foil and PLA (*14*, *40*). This study mainly focused on the cell compatibility of MoO_x flakes and Alg-Na gel electrolyte; the extraction solutions with different concentrations were used in a 96-well plate, as shown in Fig. 6A. The human endometrial adenocarcinoma (HEC-1-A) cells were selected because they are suitable for short-term and long-term compatibility test. Viability data and fluorescence images of the cells at different incubation times are shown in Fig. 6 (B and C) and figs. S16 and S17, respectively. It is noted that the existence of trace amounts (<50 μg ml^{-1}) of MoO_x flakes can enhance the growth ability of HEC-1-A cells, consistent with the reported results (*40*). The cellular density of HEC-1-A cells is obviously increased with increasing incubation time. Moreover, fluorescence images show no obvious changes in the corresponding period (24, 48, and 72 hours). All results are in agreement with those of high relative viability of the cultured HEC-1-A cells assessed by a cellular viability [MTT (3-(4,5-dimethylthiahiazol (-2-yl)-2,5-diphenytetrazolium bromide)] assay test.

Figure 6D shows the dissolution process of the encapsulated biodegradable supercapacitors (edge, PLA polymer; outside, starch paper) in PBS solution at different stages. The dimension of each MoO_x electrode is 1.0 cm × 1.0 cm, with a thickness of about 30 μm

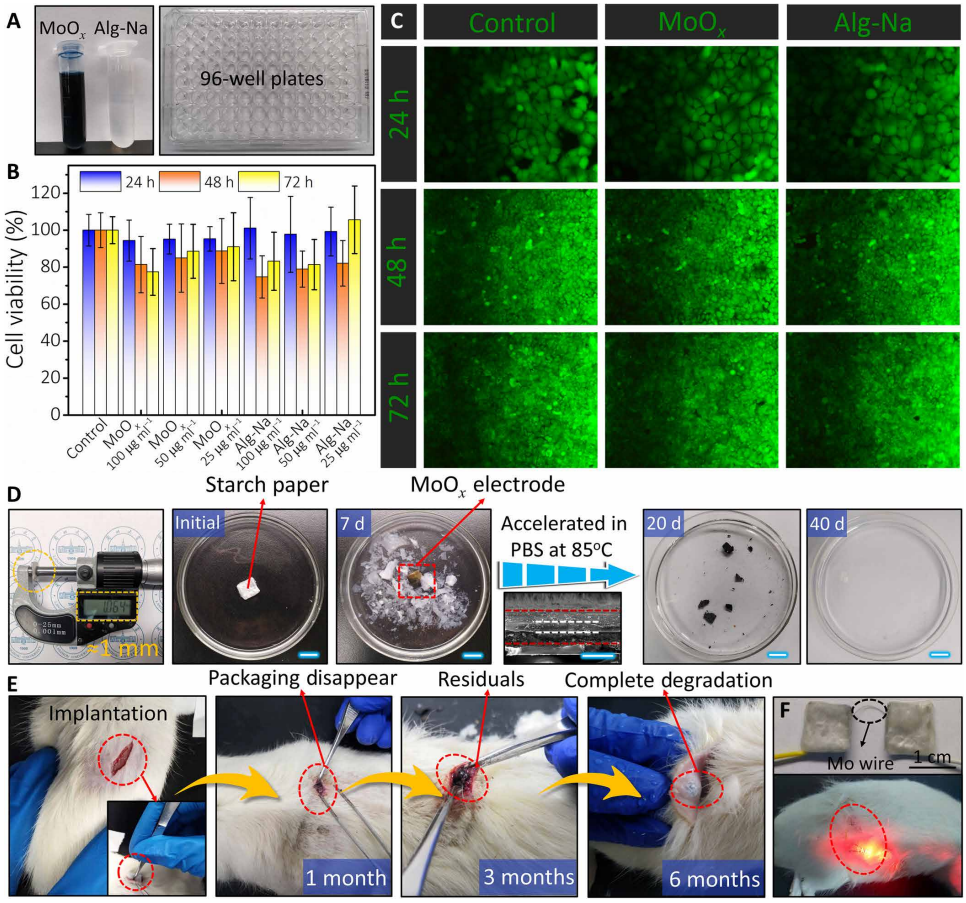

Fig. 6. Biocompatibility and degradation evaluation in vitro and in vivo. (**A**) Photographs of the human endometrial adenocarcinoma (HEC-1-A) cells cultured in 96-well plates. (**B**) Cell viability of MoO_x and Alg-Na over 24, 48, and 72 hours calculated as the fraction of total living cells. (**C**) Fluorescence images show cell viability at different times; green (calcein-AM) represents live HEC-1-A cells. (**D**) Photographs of the encapsulated supercapacitor implant with ~1 mm thickness at various dissolution stages in PBS solution. Scale bars, 1 cm. Inset below the arrow is a cross-sectional SEM image of the assembled supercapacitor implant without encapsulating. Scale bars, 30 μm. A detailed encapsulation process is presented in Materials and Methods. (**E**) In vivo degradation evaluation of the supercapacitor implant in the subcutaneous area of SD rats. (**F**) Encapsulated supercapacitor implants in series connected with the biodegradable Mo wire and a red LED light powered by the implanted supercapacitors in series. Photo credit: Hongwei Sheng, Lanzhou University.

for the biodegradable supercapacitor device (inset of Fig. 6D). After encapsulation, the total thickness and weight of each biodegradable supercapacitor are ~1 mm and 100 mg, respectively, including 30 mg of MoO_x electrode (two pieces), 70 mg of electrolyte, and encapsulated materials (PLA/starch paper; fig. S18, A and B), demonstrating a small-sized and lightweight feature of the integrated biodegradable supercapacitors. The external starch paper is degraded first within 10 days (fig. S19), followed by the disintegration of the biodegradable supercapacitor device. Meanwhile, as the dissolution proceeded, MoO_x electrodes and Alg-Na electrolyte partially dissolved because of the thin packaging layer. The remaining materials need additional 30 days to completely disappear via an accelerated experiment at an elevated temperature (85°C).

Moreover, the biodegradability of the supercapacitor as an implant was carried out in vivo. The encapsulated biodegradable supercapacitor implants (dimension, 1.0 cm × 1.0 cm × 0.1 cm) were implanted subcutaneously in the dorsal side of SD rats (Fig. 6E). In the degradation process, the external packaging layer was fully resorbed by the SD rat through metabolism after a month, along with the leakage of inner MoO_x flakes and electrolyte from the edges of the broken implant. Then, residuals of the supercapacitor implant could be observed in the subdermal region after 3 months, followed by the complete dissolution to disappear at a period of 6 months. No inflammatory response was observed during the device degradation. Compared to the in vitro process, the in vivo degradation rate is slower, which can be attributed to the differences in the liquid environments and circulation conditions. Furthermore, we used the biodegradable supercapacitor implant (two serially connected supercapacitors) to power implantable electronics. The supercapacitor implant was implanted in the dorsal subcutaneous region of an SD rat. After charging, a red LED light (threshold voltage, 1.5 V) can be lighted up successfully (Fig. 6F). Likewise, it can also readily power an electronic thermometer in PBS solution in vitro (fig. S17C), further illustrating its capability as a fully biodegradable power source for future BIMEs.

DISCUSSION

In conclusion, this work successfully developed a flexible, biodegradable and bioabsorbable, high-performance supercapacitor

implant. Two-dimensional, defective amorphous MoO_x flakes, which are grown in situ on water-soluble Mo foil as binder-free pseudocapacitive electrodes via one-step electrochemical oxidation, render the high performance of the supercapacitor implant. The supercapacitor is lightweight and has a thin structure, excellent flexibility, and high charge storage performances, including ultrahigh areal capacitance and energy density. In vitro and in vivo biodegradation and cytotoxicity evaluations demonstrate that all supercapacitor implants have excellent biocompatibility and biodegradability. The operating and degradation life span of the supercapacitor implant could be designed into a wide range by adopting proper encapsulation strategies. The supercapacitor implant can be entirely biodegraded in PBS and bioabsorbed by SD rats after implantation. These results shed light on future biodegradable and bioabsorbable implantable bioelectronics and could lead to important implications in other areas, such as hardware security.

MATERIALS AND METHODS

Preparation of the MoO_x electrode

Before synthesis, the high-purity Mo foils (20 μm for electrochemical and dissolution experiments and 10 μm for implantation experiments) were polished on SiC (1200 mesh) paper and cleaned with 2 M HCl, followed by ultrasonication for 10 min in acetone, ethanol, and deionized (DI) water, respectively. The cleaned Mo foils were anodized in a three-electrode configuration, consisting of Mo foil as the working electrode, platinum (Pt) plate as the counter electrode, Ag/AgCl as the reference electrode, and 1 M NaCl as the electrolyte solution at room temperature. The working electrode was subjected to CV at the same scan rate (0.1 V s^{-1}) in a positive potential window (0 to 0.8 V) for 150 cycles. After cycling, the obtained MoO_x samples were carefully rinsed with absolute ethanol and DI water for several times. The MoO_3 samples were obtained by annealing MoO_x samples in air at 500°C for 3 hours with a heating rate of 5°C min^{-1}.

Fabrication and encapsulation of supercapacitors

Alg-Na gel electrolyte was synthesized by adding 0.8 g of Alg-Na powder to 20 ml of DI water with stirring in a water bath at 70°C until the solution became colorless and transparent. Before using, the solution was stored at room temperature for 1 day, removing the resulting gas cavities from the gel. The prepared Alg-Na gel electrolyte was coated onto MoO_x electrodes and then solidified for 1 hour. Symmetric biodegradable supercapacitors were assembled using a pair of MoO_x electrodes with Alg-Na gel electrolyte, controlling to 1 cm × 1 cm. The edges of biodegradable supercapacitors were encapsulated with PVA hydrogel and PLA polymer to carry out in vitro tests, respectively. The PVA hydrogel and PLA polymer solutions were synthesized as follows: (i) 1 g of PVA powders (molecular weight of 100,000, hydrolyzed; Sigma-Aldrich) was dissolved in 10 ml of DI water under stirring at 80°C. (ii) PLA solution with 5 weight % (wt %) was achieved by mixing with PLA granules (Jinan Daigang Biomaterial Co., Ltd., China) and trichloromethane. The encapsulated biodegradable supercapacitors were characterized after drying out completely. For the electrical connection, a copper (Cu) tape was connected to one side of the electrodes with the assistance of a small amount of silver paste and epoxy to alleviate the corrosion of PBS in connection between Cu tape and electrodes, guaranteeing the operational stability of tests in liquid environment.

The encapsulation involves coating only the thin edges of biodegradable supercapacitor devices with PVA hydrogel and PLA polymer precursors and then solidifying to serve as the encapsulation layer to enable short- and long-term functional timeline. For in vivo animal experiment, an additional encapsulation of a starch paper covering the supercapacitor device was used to further control the operational lifetime of devices. Starch paper is a commonly used glutinous rice paper produced from corn starch. After the device was first encapsulated on its edges with PLA polymer, a thin starch film (area, 4 cm × 4 cm; weight, 50 mg; thickness, ~20 μm) directly bonded to the device, thus rendering a uniform encapsulation over the device.

Dissolution tests for MoO_x electrodes and Alg-Na gel film

To investigate the dissolution process and dynamics of MoO_x electrodes and Alg-Na gel electrolyte film, we performed a series of dissolution tests in 10 ml of PBS (10 mM, pH 7.4) at different temperatures. Typically, 10 mM PBS solution is prepared as follows: 8.00 g of NaCl, 0.20 g of KCl, 2.90 g of $Na_2HPO_4{\cdot}12H_2O$, and 0.20 g of KH_2PO_4 were dissolved in 1 liter of DI water under stirring at room temperature. In the dissolution tests, MoO_x electrodes were regularly taken out from PBS solution, rinsed in DI water, and then dried to measure the weight. After that, a fresh PBS solution was used to ensure the same chemical environment every day. For MoO_x electrodes, the dissolution process was carried out in PBS solution (10 mM, pH 7.4) at body temperature (37°C) and room temperature (22°C) for 180 days, respectively. The freestanding Alg-Na film was prepared by casting Alg-Na gel electrolyte on a homemade glass mold (depth, ~1 mm) at room temperature and then peeled off. The dissolution process of Alg-Na film (1 cm × 2 cm) was performed in PBS solution (10 mM, pH 7.4) at an elevated temperature (60°C) for 2 hours.

Cell culture

HEC-1-A cells (5×10^3 cells per well, 100 μl per well) were cultured in Dulbecco's modified Eagle's medium (DMEM; Gibco) containing 10% fetal bovine serum (Gibco) and 1% penicillin/streptomycin (Gibco). HEC-1-A cells were incubated at a humidity atmosphere containing 5% CO_2 at 37°C for 24, 48, and 72 hours. For MoO_x flakes and Alg-Na powder sterilized by UV light, aqueous extractions with different concentrations (0, 0.8, 1.6, 3.125, 6.25, 12.5, 25, 50, 100, and 200 μg ml^{-1}) were synthesized for HEC-1-A cell culture. Cell viability is equal to the absorbance ratio of the experimental group and the control group.

Cellular viability test (MTT) assay

Cell viability and proliferation of HEC-1-A cells were evaluated by MTT assay. After coculturing for 24, 48, and 72 hours, the culture media of HEC-1-A cells were replaced with 100 μl of DMEM and 10 μl of MTT solution (5 mg ml^{-1}) and then incubated for 4 hours in a humidified atmosphere with 5% CO_2 at 37°C. The supernatant solution was replaced using 150 μl of dimethyl sulfoxide (DMSO) to dissolve the deposited purple formazan granules. A multimode microplate reader (FlexStation 3, Molecular Devices, USA) was used to measure the optical density value at a wavelength of 490 nm. Three parallel control cells were applied to each group.

Cell morphology and immunofluorescence staining

After the supernatants were removed, the cells were washed with PBS (pH 7.4) three times at room temperature and then stained with calcein-AM (30 min) and propidium iodide (15 min), respectively.

Fluorescence images were taken using fluorescence microscopy (U-LH50HG, Olympus, Japan).

In vivo study

The male SD rats (white, 200 to 220 g, 40 days) were purchased from the Animal Center of Medical College of Lanzhou University (People's Republic of China), housed in a temperature-controlled environment (22 ± 1°C) under standard 12-hour light/dark conditions, and received food and water ad libitum. Animals were used only once and received good care and humane treatment. We followed the protocol approved by the Ethics Committee of Lanzhou University (approval reference no. SYXK Gan 2009–0005). Our investigation conformed to Lanzhou University animal policies and the Association for Assessment and Accreditation of Laboratory Animal Care accreditation standards. All efforts were made to minimize animal suffering and to reduce the number of animals used.

Before the surgery, the rats were fed to the new experimental environment for 1 week. The anesthesia procedure of SD rats began with the intake of isoflurane gas (4% in pure medical-grade oxygen), followed by the injection of 1% sodium pentobarbital (intraperitoneal, 40 mg kg^{-1}) for anesthesia induction and maintenance, respectively. The encapsulated supercapacitors were sterilized by UV and 75% alcohol for 1 hour and then implanted subcutaneously in the back of SD rats. After the biodegradable supercapacitors entirely disappeared from view, the SD rat was raised for another week and then euthanized.

Material characterization

The morphology of the samples was observed on a field-emission SEM (FEI-SEM, Apreo S). Lattice-resolved TEM and SAED patterns were achieved on FEI Tecnai F30 at 300 kV. The crystal structure was obtained by grazing incidence XRD (Philips, X'Pert Pro, Cu Kα; 0.154056 nm) and Raman spectroscopy (JY-HR800 micro-Raman) using a 532-nm wavelength yttrium aluminum garnet (YAG). laser with a laser spot diameter of ~600 nm. The chemical composition was collected using XPS (PHI-5702, Mg KR x-ray; 1253.6 eV). Oxygen vacancies were determined by ESR (X-band Bruker ER200D) and TGA (PerkinElmer Instruments, TG/DTA module) within the temperature range of 10° to 500°C in air and argon atmosphere, respectively. Absorption spectra were obtained on a UV-Vis spectrophotometer (U-3900H, HITACHI).

Electrochemical measurements

Electrochemical measurements (CHI 660E) were accomplished in a three-electrode configuration containing 1 M NaCl aqueous electrolyte, as detailed previously. CV and GCD tests were performed at various scan rates and current densities, respectively. EIS was conducted at the open circuit potential with frequencies ranging from 0.1 Hz to 1 MHz (the amplitude was 5 mV). EIS was fitted with ZView software to analyze electrochemical reactions and interface properties.

SUPPLEMENTARY MATERIALS

Supplementary material for this article is available at http://advances.sciencemag.org/cgi/content/full/7/2/eabe3097/DC1

REFERENCES AND NOTES

1. S.-W. Hwang, H. Tao, D.-H. Kim, H. Cheng, J.-K. Song, E. Rill, M. A. Brenckle, B. Panilaitis, S. M. Won, Y.-S. Kim, Y. M. Song, K. J. Yu, A. Ameen, R. Li, Y. Su, M. Yang, D. L. Kaplan, M. R. Zakin, M. J. Slepian, Y. Huang, F. G. Omenetto, J. A. Rogers, A physically transient form of silicon electronics. *Science* **337**, 1640–1644 (2012).
2. S.-W. Hwang, J.-K. Song, X. Huang, H. Cheng, S.-K. Kang, B. H. Kim, J.-H. Kim, S. Yu, Y. Huang, J. A. Rogers, High-performance biodegradable/transient electronics on biodegradable polymers. *Adv. Mater.* **26**, 3905–3911 (2014).
3. K. K. Fu, Z. Wang, J. Dai, M. Carter, L. Hu, Transient electronics: Materials and devices. *Chem. Mater.* **28**, 3527–3539 (2016).
4. X. Chen, Y. J. Park, M. Kang, S.-K. Kang, J. Koo, S. M. Shinde, J. Shin, S. Jeon, G. Park, Y. Yan, M. R. MacEwan, W. Z. Ray, K.-M. Lee, J. A. Rogers, J.-H. Ahn, CVD-grown monolayer MoS_2 in bioabsorbable electronics and biosensors. *Nat. Commun.* **9**, 1690 (2018).
5. C.-H. Lai, D. S. Ashby, N. H. Bashian, J. Schoiber, T.-C. Liu, G. S. Lee, S.-Y. Chen, P.-W. Wu, B. C. Melot, B. S. Dunn, Designing the charge storage properties of Li-exchanged sodium vanadium fluorophosphate for powering implantable biomedical devices. *Adv. Energy Mater.* **9**, 1900226 (2019).
6. J. S. Ho, A. J. Yeh, E. Neofytou, S. Kim, Y. Tanabe, B. Patlolla, R. E. Beygui, A. S. Y. Poon, Wireless power transfer to deep-tissue microimplants. *Proc. Natl. Acad. Sci. U.S.A.* **111**, 7974–7979 (2014).
7. J. Kim, J. Seo, D. Jung, T. Lee, H. Ju, J. Han, N. Kim, J. Jeong, S. Cho, J. H. Seol, J. Lee, Active photonic wireless power transfer into live tissues. *Proc. Natl. Acad. Sci. U.S.A.* **117**, 16856–16863 (2020).
8. B. Shi, Z. Liu, Q. Zheng, J. Meng, H. Ouyang, Y. Zou, D. Jiang, X. Qu, M. Yu, L. Zhao, Y. Fan, Z. L. Wang, Z. Li, Body-integrated self-powered system for wearable and implantable applications. *ACS Nano* **13**, 6017–6024 (2019).
9. Y. Zou, P. Tan, B. Shi, H. Ouyang, D. Jiang, Z. Liu, H. Li, M. Yu, C. Wang, X. Qu, L. Zhao, Y. Fan, Z. L. Wang, Z. Li, A bionic stretchable nanogenerator for underwater sensing and energy harvesting. *Nat. Commun.* **10**, 2695 (2019).
10. R. Li, H. Qi, Y. Ma, Y. Deng, S. Liu, Y. Jie, J. Jing, J. He, X. Zhang, L. Wheatley, C. Huang, X. Sheng, M. Zhang, L. Yin, A flexible and physically transient electrochemical sensor for real-time wireless nitric oxide monitoring. *Nat. Commun.* **11**, 3207 (2020).
11. L. Yin, X. Huang, H. Xu, Y. Zhang, J. Lam, J. Cheng, J. A. Rogers, Materials, designs, and operational characteristics for fully biodegradable primary batteries. *Adv. Mater.* **26**, 3879–3884 (2014).
12. X. Wang, W. Xu, P. Chatterjee, C. Lv, J. Popovich, Z. Song, L. Dai, M. Y. S. Kalani, S. E. Haydel, H. Jiang, Food-materials-based edible supercapacitors. *Adv. Mater. Technol.* **1**, 1600059 (2016).
13. C. Chen, Y. Zhang, Y. Li, J. Dai, J. Song, Y. Yao, Y. Gong, I. Kierzewski, J. Xie, L. Hu, All-wood, low tortuosity, aqueous, biodegradable supercapacitors with ultra-high capacitance. *Energ. Environ. Sci.* **10**, 538–545 (2017).
14. G. Lee, S.-K. Kang, S. M. Won, P. Gutruf, Y. R. Jeong, J. Koo, S.-S. Lee, J. A. Rogers, J. S. Ha, Fully biodegradable microsupercapacitor for power storage in transient electronics. *Adv. Energy Mater.* **7**, 1700157 (2017).
15. M. Hu, J. Wang, J. Liu, P. Wang, Y. Feng, H. Wang, N. Nie, Y. Wang, Y. Huang, A flour-based one-stop supercapacitor with intrinsic self-healability and stretchability after self-healing and biodegradability. *Energy Storage Mater.* **21**, 174–179 (2019).
16. H. Lee, G. Lee, J. Yun, K. Keum, S. Y. Hong, C. Song, J. W. Kim, J. H. Lee, S. Y. Oh, D. S. Kim, M. S. Kim, J. S. Ha, Facile fabrication of a fully biodegradable and stretchable serpentine-shaped wire supercapacitor. *Chem. Eng. J.* **366**, 62–71 (2019).
17. H. Li, C. Zhao, X. Wang, J. Meng, Y. Zou, S. Noreen, L. Zhao, Z. Liu, H. Ouyang, P. Tan, M. Yu, Y. Fan, Z. L. Wang, Z. Li, Fully bioabsorbable capacitor as an energy storage unit for implantable medical electronics. *Adv. Sci.* **6**, 1801625 (2019).
18. P. Roy, S. Berger, P. Schmuki, TiO_2 nanotubes: Synthesis and applications. *Angew. Chem. Int. Ed.* **50**, 2904–2939 (2011).
19. M. Vasilopoulou, A. M. Douvas, D. G. Georgiadou, L. C. Palilis, S. Kennou, L. Sygellou, A. Soultati, I. Kostis, G. Papadimitropoulos, D. Davazoglou, P. Argitis, The influence of hydrogenation and oxygen vacancies on molybdenum oxides work function and gap states for application in organic optoelectronics. *J. Am. Chem. Soc.* **134**, 16178–16187 (2012).
20. J. Chen, S. Han, H. Zhao, J. Bai, L. Wang, G. Sun, Z. Zhang, X. Pan, J. Zhou, E. Xie, Robust wire-based supercapacitors based on hierarchical α-MoO_3 nanosheet arrays with well-aligned laminated structure. *Chem. Eng. J.* **320**, 34–42 (2017).
21. M. Dieterle, G. Weinberg, G. Mestl, Raman spectroscopy of molybdenum oxides part I. Structural characterization of oxygen defects in MoO_{3-x} by DR UV/VIS, Raman spectroscopy and X-ray diffraction. *Phys. Chem. Chem. Phys.* **4**, 812–821 (2002).
22. H.-S. Kim, J. B. Cook, H. Lin, J. S. Ko, S. H. Tolbert, V. Ozolins, B. Dunn, Oxygen vacancies enhance pseudocapacitive charge storage properties of MoO_{3-x}. *Nat. Mater.* **16**, 454–460 (2017).
23. K. K. Upadhyay, T. Nguyen, T. M. Silva, M. J. Carmezim, M. F. Montemor, Electrodeposited MoO_x films as negative electrode materials for redox supercapacitors. *Electrochim. Acta* **225**, 19–28 (2017).
24. J. Baltrusaitis, B. Mendoza-Sanchez, V. Fernandez, R. Veenstra, N. Dukstiene, A. Roberts, N. Fairley, Generalized molybdenum oxide surface chemical state XPS determination via informed amorphous sample model. *Appl. Surf. Sci.* **326**, 151–161 (2015).
25. J. G. Choi, L. T. Thompson, XPS study of as-prepared and reduced molybdenum oxides. *Appl. Surf. Sci.* **93**, 143–149 (1996).

26. H. Bai, W. Yi, J. Li, G. Xi, Y. Li, H. Yang, J. Liu, Direct growth of defect-rich MoO_{3-x} ultrathin nanobelts for efficiently catalyzed conversion of isopropyl alcohol to propylene under visible light. *J. Mater. Chem. A* **4**, 1566–1571 (2016).
27. Q. Lu, Y. Yang, J. Feng, X. Wang, Oxygen-defected molybdenum oxides hierarchical nanostructure constructed by atomic-level thickness nanosheets as an efficient absorber for solar steam generation. *Sol. RRL* **3**, 1800277 (2019).
28. Y. Zhang, L. Tao, C. Xie, D. Wang, Y. Zou, R. Chen, Y. Wang, C. Jia, S. Wang, Defect engineering on electrode materials for rechargeable batteries. *Adv. Mater.* **32**, e1905923 (2020).
29. M. Petrova, M. Bojinov, S. Zanna, P. Marcus, Mechanism of anodic oxidation of molybdenum in nearly-neutral electrolytes studied by electrochemical impedance spectroscopy and X-ray photoelectron spectroscopy. *Electrochim. Acta* **56**, 7899–7906 (2011).
30. W. A. Badawy, F. M. Al-Kharafi, Corrosion and passivation behaviors of molybdenum in aqueous solutions of different pH. *Electrochim. Acta* **44**, 693–702 (1998).
31. J. Chang, M. Jin, F. Yao, T. H. Kim, V. T. Le, H. Yue, F. Gunes, B. Li, A. Ghosh, S. Xie, Y. H. Lee, Asymmetric supercapacitors based on graphene/MnO_2 nanospheres and graphene/MoO_3 nanosheets with high energy density. *Adv. Funct. Mater.* **23**, 5074–5083 (2013).
32. X. Xiao, T. Ding, L. Yuan, Y. Shen, Q. Zhong, X. Zhang, Y. Cao, B. Hu, T. Zhai, L. Gong, J. Chen, Y. Tong, J. Zhou, Z. L. Wang, WO_{3-x}/MoO_{3-x} core/shell nanowires on carbon fabric as an anode for all-solid-state asymmetric supercapacitors. *Adv. Energy Mater.* **2**, 1328–1332 (2012).
33. X. Zhang, Q. Fu, H. Huang, L. Wei, X. Guo, Silver-quantum-dot-modified MoO_3 and MnO_2 paper-like freestanding films for flexible solid-state asymmetric supercapacitors. *Small* **15**, 1805235 (2019).
34. T. Tsumura, M. Inagaki, Lithium insertion/extraction reaction on crystalline MoO_3. *Solid State Ion.* **104**, 183–189 (1997).
35. H. Li, Z. Tang, Z. Liu, C. Zhi, Evaluating flexibility and wearability of flexible energy storage devices. *Joule* **3**, 613–619 (2019).
36. H. Hu, Z. Pei, H. Fan, C. Ye, 3D interdigital Au/MnO_2/Au stacked hybrid electrodes for on-chip microsupercapacitors. *Small* **12**, 3059–3069 (2016).
37. D. P. Dubal, D. Aradilla, G. Bidan, P. Gentile, T. J. S. Schubert, J. Wimberg, S. Sadki, P. Gomez-Romero, 3D hierarchical assembly of ultrathin MnO_2 nanoflakes on silicon nanowires for high performance micro-supercapacitors in Li-doped ionic liquid. *Sci. Rep.* **5**, 09771 (2015).
38. K. V. Rajagopalan, Molybdenum: An essential trace-element in human-nutrition. *Annu. Rev. Nutr.* **8**, 401–427 (1988).
39. S.-W. Hwang, G. Park, C. Edwards, E. A. Corbin, S.-K. Kang, H. Cheng, J.-K. Song, J.-H. Kim, S. Yu, J. Ng, J. E. Lee, J. Kim, C. Yee, B. Bhaduri, Y. Su, F. G. Omennetto, Y. Huang, R. Bashir, L. Goddard, G. Popescu, K.-M. Lee, J. A. Rogers, Dissolution chemistry and biocompatibility of single-crystalline silicon nanomembranes and associated materials for transient electronics. *ACS Nano* **8**, 5843–5851 (2014).
40. X. Huang, D. Wang, Z. Yuan, W. Xie, Y. Wu, R. Li, Y. Zhao, D. Luo, L. Cen, B. Chen, H. Wu, H. Xu, X. Sheng, M. Zhang, L. Zhao, L. Yin, A fully biodegradable battery for self-powered transient implants. *Small* **14**, 1800994 (2018).

Acknowledgments

Funding: This work was funded by the National Natural Science Foundation of China (61874166 and U1832149), Natural Science Foundation of Gansu Province (18JR3RA292), and the Science and Technology Program of Qinghai Province (2020-HZ-809). **Author contributions:** W.L., K.W., C.Y., H.S., and Jingjing Zhou designed the research. H.S., B.L., and X.Z. developed the supercapacitor and tested its electrochemical performance. H.S., Jingjing Zhou, J.L., and Y.H. assisted in performing the cell experiment and implantation experiment. E.X., Jinyuan Zhou, and Q.S. helped with data discussion. H.S., W.L., K.W., and C.Y. wrote and reviewed the paper. All authors contributed to the discussion of results and approved the final version. **Competing interests:** The authors declare that they have no competing interests. **Data and materials availability:** All data needed to evaluate the conclusions in the paper are present in the paper and/or the Supplementary Materials. Additional data related to this paper may be requested from the authors.

Submitted 14 August 2020
Accepted 12 November 2020
Published 8 January 2021
10.1126/sciadv.abe3097

Citation: H. Sheng, J. Zhou, B. Li, Y. He, X. Zhang, J. Liang, J. Zhou, Q. Su, E. Xie, W. Lan, K. Wang, C. Yu, A thin, deformable, high-performance supercapacitor implant that can be biodegraded and bioabsorbed within an animal body. *Sci. Adv.* **7**, eabe3097 (2021).